RSC Applied Interfaces

ROYAL SOCIETY OF CHEMISTRY

PAPER

View Article Online
View Journal | View Issue

Cite this: *RSC Appl. Interfaces*, 2025, **2**, 397

Uncovering interfacial electron transfer kinetics of WO_3 biophotoelectrodes for food waste treatment†

Chun Hong Mak,[ace] Yong Peng,[ae] Man Hin Chong,[a] Jinhua Mou,[a] Guohua Jia,[f] Shella Permatasari Santoso,[g] Wenxin Niu,[h] Duu-Jong Lee,*[c] Chang-Ping Yu,[i] Carol Sze Ki Lin[a] and Hsien-Yi Hsu*[abde]

An effective approach to enhance bioelectrochemical systems' performance involves leveraging semiconductors' light-harvesting capabilities alongside the catalytic properties of bacteria. Here, we demonstrate a food waste removal method using the integration of *Shewanella oneidensis* MR-1 with a tungsten(VI) oxide (WO_3) nanoplate photoanode in a solar-assisted microbial photoelectrochemical cell (S-MPEC) combined with silicon-based photovoltaics (SiPV). The S-MPEC integrates the technologies of bioelectrochemical cells with photoelectrochemical cells (PEC) to enhance the degradation of food waste. The bare WO_3 photoelectrode exhibits a photocurrent of 0.749 A m^{-2} at 0.8 V under visible light, whereas the WO_3-MR-1 biophotoelectrode reveals a significantly higher photocurrent of 2.94 A m^{-2}. Under visible light exposure at an intensity of less than 100 mW cm^{-2}, the power densities of the WO_3 photoelectrode with and without MR-1 bacterial coating are 2.36 W m^{-2} and 0.599 W m^{-2}, respectively. To further improve performance, the S-MPEC was connected with a SiPV. This combined system, PV-S-MPEC, achieved a power density of 21.99 W m^{-2} and a chemical oxygen demand (COD) removal rate of 8167 mg L^{-1} per day, demonstrating its effectiveness in degrading food waste hydrolysate. Additionally, the study of heterogeneous electron transfer kinetics indicated that the WO_3-MR-1 system exhibits more efficient diffusion coefficients and enhanced rate constants for reduction and oxidation reactions. These findings highlight the significant impact of photoexcited charge carriers on degradation performance in this complex hybrid electricigen system, underscoring its potential for developing S-MPECs for waste degradation. This study also demonstrates significant potential for reducing environmental impact through enhanced COD removal rates and energy-efficient waste processing, making it a viable solution for large-scale applications in urban waste management.

Received 15th August 2024,
Accepted 17th September 2024

DOI: 10.1039/d4lf00291a

rsc.li/RSCApplInter

1. Introduction

Biomass is a vital fuel source with numerous applications driven by advanced methods.[1–5] Food waste, a significant component of biomass derived from human activities, constitutes a considerable portion of municipal solid waste.[6] Currently, most food waste is managed through traditional methods such as landfilling, composting, and incineration. These practices can contaminate groundwater, attract pests, and emit toxic gases. Additionally, they are unsustainable and economically inefficient, as they do not fully utilize the valuable nutrients and energy stored in food waste. The microbial fuel cell (MFC) represents a promising anaerobic waste treatment technology that employs microorganisms as catalysts to generate electricity from various organic wastes, including domestic and industrial wastewater and excess sludge.[7–12] MFCs can efficiently produce clean, direct electricity while simultaneously removing organic matter, offering a more sustainable and practical approach to waste management.

[a] *School of Energy and Environment, City University of Hong Kong, Kowloon Tong, Hong Kong SAR. E-mail: sam.hyhsu@cityu.edu.hk*
[b] *Department of Materials Science and Engineering, City University of Hong Kong, Kowloon Tong, Hong Kong SAR*
[c] *Department of Mechanical Engineering, City University of Hong Kong, Kowloon Tong, Hong Kong SAR. E-mail: tuclee@cityu.edu.hk*
[d] *Centre for Functional Photonics (CFP), City University of Hong Kong, Kowloon Tong, Hong Kong SAR*
[e] *Shenzhen Research Institute of City University of Hong Kong, Shenzhen, 518057, China*
[f] *Curtin Institute of Functional Molecules and Interfaces, School of Molecular and Life Sciences, Curtin University, GPO Box U1987, Perth, WA 6845, Australia*
[g] *Department of Chemical Engineering, Faculty of Engineering, Widya Mandala Surabaya Catholic University, Kalijudan No. 37, Surabaya 60114, East Java, Indonesia*
[h] *State Key Laboratory of Electroanalytical Chemistry, Changchun Institute of Applied Chemistry, Chinese Academy of Sciences, 5625 Renmin Street, Changchun, Jilin 130022, P. R. China*
[i] *Graduate Institute of Environmental Engineering, National Taiwan University, Taipei, 10617, Taiwan*

† Electronic supplementary information (ESI) available. See DOI: https://doi.org/10.1039/d4lf00291a

The relatively low power density of microbial fuel cells (MFC) for industrial applications remains challenging. Noticeably, the combination of bioelectrochemistry with photoelectrochemistry presents a promising approach. One such innovative method is the solar-assisted microbial photoelectrochemical cell (S-MPEC). Specifically, S-MPECs utilize a photo-active semiconductor as the photoelectrode, which can significantly boost the anodic potential under solar irradiation, enhancing anodic reactions. Using photoanodes combined with *Shewanella oneidensis* MR-1 (MR-1), a model electrogenic microorganism, has garnered significant interest. A pioneering example of a synergistic semiconductor/ electricigen system was first demonstrated by Qian *et al.*, where the development of a Fe_2O_3 nanowire photoelectrode facilitated active electron transfer at the Fe_2O_3/cell interface. This transfer occurred *via* a significant c-type cytochrome outer membrane protein, resulting in increased photocurrent upon irradiation.[13]

Tungsten(VI) oxide (WO_3) has been identified as a robust candidate for photoelectrodes.[14] Recently, WO_3 has been utilized as a bioanode in MFCs due to its biocompatibility and enhanced conductivity, promoting improved adhesion and charge transfer between bacteria and the electrode material.[15] However, an in-depth investigation of the heterogeneous electron transfer dynamics and the interaction between photoelectrode and bacteria remains largely unexplored. Our work extends these findings by employing WO_3 as a superior photoanode material. Our research confirms the synergistic effects observed in earlier studies and quantifies the increase in photocurrent and degradation rates, providing a clearer understanding of the kinetics involved. This study employs electrochemical methods to explore heterogeneous electron transfer and electrochemical redox activity. Furthermore, we explore the integration of this system using silicon-based photovoltaics (SiPV) with S-MPEC. This novel addition significantly enhances both the anodic electron transfer and the COD removal efficiency beyond the capabilities previously reported in the literature.[16–22] This advancement offers a promising direction for scaling up bio-photoelectrochemical systems for practical waste management and renewable energy production applications. The findings from this research lay a solid foundation for developing highly efficient S-MPECs that generate electricity and simultaneously address wastewater treatment and solar fuel production.

2. Methodology

2.1. Preparation of tungsten(VI) oxide (WO_3) photoelectrode

Tungsten(VI) oxide (WO_3) was synthesized on fluorine-doped tin oxide (FTO) glass using a nanoplate substrate *via* a peroxotungstate reduction reaction, following a method previously described in the literature.[23–25] 0.15 g of ammonium oxalate ($(NH_4)_2C_2O_4$) and 0.4 g of sodium tungstate dihydrate (Na_2WO_4) were in 33 mL of ultrapure water followed by the addition of 9 mL of 37% hydrochloric acid (HCl). Subsequently, 8 mL of 37% hydrogen peroxide (H_2O_2) was introduced into the mixture and allowed to react for 10 minutes. Then, 30 mL of ethanol was added and stirred for 10 minutes to achieve a clear and stable solution.

The FTO glass substrates were immersed in the resultant solution, with the conductive side facing upward, and the synthesis was conducted at a constant temperature of 85 °C in a water bath, with a heating rate of 5 °C per minute, followed by natural cooling. After synthesis, the coated FTO glass was rinsed with ultrapure water for 1 minute and dried at 50 °C for 10 hours. The samples were then annealed in a muffle furnace at 500 °C for 2 hours and allowed to cool at a rate of 1 °C per minute, forming a pale olive-colored WO_3 nanoplate on the FTO.

To complete the assembly of the photoelectrodes, titanium (Ti) wires were affixed to the FTO surfaces using silver glue to ensure electrical connectivity. The wires were then encapsulated with epoxy resin to protect the connections and dried on a hot plate at 65 °C for 30 minutes.

2.2. Characterization of WO_3

The morphological characteristics of the WO_3 samples were examined using a ZEISS EVO MA10 scanning electron microscope (SEM) operating at 15 kV. The crystallographic properties were investigated through X-ray diffraction (XRD) analysis, employing a PANalytical X'Pert^3 X-ray diffractometer. XRD patterns were collected over a 2θ range of 20 to 60 degrees, utilizing a voltage of 40 kV and a current of 40 mA with Cu-Kα radiation (wavelength of 1.54 Å).

The specimens underwent a sequential fixation and dehydration protocol for imaging studies of samples coated with MR-1 biofilm. Initially, the samples were fixed with 2.5% (v/v) glutaraldehyde for 20 minutes. Subsequent dehydration was achieved using an ethanol gradient, with concentrations of 50%, 70%, 80%, and 90%, and three successive exposures to 100% ethanol, each lasting 5 minutes. This step was crucial to adequately dehydrate the fixed MR-1 cells to ensure clarity in imaging. Following dehydration, the sample photoelectrodes were sputtered with gold to enhance the resolution of SEM imaging, facilitating high-resolution imaging of the biofilm morphology.

Photoluminescence (PL) spectra of the samples were recorded using a Shimadzu RF-5301 PC spectrometer equipped with a 390 nm long-pass filter. The samples were excited using an excitation wavelength of 375 nm. Additionally, time-resolved PL measurements were conducted using a time-correlated single photon counting setup from PicoQuant GmbH. For these measurements, the sample excitation was performed with a laser head delivering pulses shorter than 200 ps, with a fluence of approximately 30 nJ cm^{-2}, to study the photophysical dynamics of the samples.

2.3. Cultivation of MR-1

Luria-Bertani (LB) (*i.e.*, 10 g NaCl, 5 g yeast extract, and 10 g tryptone in 1000 mL ultrapure water) was chosen as the

medium for growing MR-1. LB was then autoclaved for 20 minutes at 120 °C for sterilization. The stock of the solutions of MR-1 from the ultralow freezer (−80 °C) was streaked to an agar plate inside the biological safety cabinet (BSC) after cooling down to room temperature and placed in the incubator at 30 °C for 12 hours. MR-1 was grown in the agar plate to 10^7 to 10^8 CFU mL^{-1}, ensuring an adequate cell density for robust biofilm formation on the electrode surface. Then MR-1 was pipetted from Petri dish to 40 mL LB medium inside BSC after cooling down. After adding MR-1, the medium was incubated in a shaker with 250 revolutions per minute (rpm) at 25 °C for 12 hours. The specimen containers with MR-1 were then stored inside 3 °C freezer and ready for use.

2.4. Solar-assisted microbial photoelectrochemical cell (S-MPEC)

A dual-chamber solar-assisted microbial photoelectrochemical cell (S-MPEC) was constructed using a 200 mL cylindrical acrylic chamber. The volumes of the anodic and cathodic chambers were 100 mL. The chambers were equipped with quartz windows to facilitate light entry. A WO_3 photoanode with an exposed area of 2.5 cm^2 was integrated into the setup.

The S-MPEC was then prepared for biological experimentation by adding LB medium to both chambers in a BSC to maintain sterility. Subsequently, 200 μL of *Shewanella oneidensis* MR-1 culture was directly pipetted into the anodic chamber. The cultivation of MR-1 within the S-MPEC was carried out under controlled conditions: the system was connected to a 1000 Ω resistor at room temperature, with a constant stirring speed of 100 rpm. This environment was maintained for 12 hours to promote the formation and incubation of the biofilm.[26] After 12 hours, gray sedimentations were found inside the andic chamber, which were MR-1. S-MPEC was then connected to an electrochemical workstation for further analysis.

2.5. PV-S-MPEC system

The operation of PV-S-MPEC is the same as that of the S-MPEC system, except that a commercially available silicon photovoltaic (PV) module delivering 3.5 V was connected with the S-MPEC. The bioanode of S-MPEC was connected to the solar cell's counter electrode (positive electrode). The counter electrode (negative electrode) of the SiPV was connected to the cathode of the S-MPEC. The output voltage was measured in the dark and under irradiation across a 10 Ω resistor connected between the counter electrode of SiPV and the cathode of the S-MPEC.

2.6. Electrochemical characterization

The electrochemical measurements within the S-MPEC were conducted using a three-electrode configuration setup. This setup included a WO_3 nanoplate electrode serving as the working electrode, an Ag/AgCl electrode saturated with 3 M potassium chloride (KCl) as the reference electrode, and a 3 cm platinum (Pt) wire as the counter electrode.

In the assembly of the S-MPEC, the as-prepared photoelectrode was positioned such that the WO_3 nanoplate faced inward toward the interior of the chamber. This orientation ensured optimal interaction between the electrode surface and the chamber's environment. The chamber was modified to maintain anaerobic conditions within the cell, which are crucial for accurately simulating specific environmental and biological processes. Two holes at the top of the S-MPEC, designed for inserting the counter and reference electrodes, were sealed with drilled stoppers. Additionally, an argon gas stream was continuously supplied to displace any oxygen present, preserving the anaerobic atmosphere. Cyclic voltammetry of S-MPEC was measured by a CHI660E electrochemical workstation.

2.7. Photoelectrochemical (PEC) measurements

All photoelectrochemical (PEC) measurements within the S-MPEC were conducted at room temperature using a CHI660E electrochemical workstation. Linear sweep voltammetry (LSV) was employed, covering a potential range from −0.2 to 1.0 V *versus* Ag/AgCl, with a sweep rate of 10 mV s^{-1}, to examine the electrochemical characteristics of the system.[27–31] Cyclic voltammetry (CV) experiments were executed at a scan rate of 1 mV s^{-1}, with a potential window from −1.0 V to 0.2 V *versus* Ag/AgCl for detailed analysis of the electrochemical processes in the bacteria/electrode interfaces. The 300 W xenon light source (6258, Newport Corporation) with 420 nm cutoff filter was used as a light source. The light intensity was precisely controlled at 100 mW cm^{-2}, with measurements verified by an optical power meter (Model 19180R, Newport Corporation).[32–35] Amperometric measurements were performed at a constant applied voltage of 0.8 V *versus* Ag/AgCl to evaluate the system's long-term stability. This measurement was sustained over 24 hours under continuous illumination at 100 mW cm^{-2}, providing critical insights into the endurance and operational reliability of the S-MPEC under simulated operational conditions.[36–41]

2.8. Preparation of food waste hydrolysate

Food waste was collected from a university canteen and stored at −20 °C before enzymatic hydrolysis. Briefly, 1 kg of food waste was blended with 500 mL of deionised water using a kitchen blender, and then subjected to enzymatic hydrolysis using 1% (v/m, enzyme/food waste) dosage of glucoamylase, protease, and cellulase (Sunson, China). The hydrolysis broth was centrifuged at 8000 × *g* for 30 min, and the supernatant was collected, filtered using 1 μm pore size of filter paper, and stored at −20 °C until further processing. The final glucose concentrations are 98 ± 20 g L^{-1}. The food waste hydrolysate was sterilise-filtered by a 0.22 μm pore size membrane filter (Sartorius, Germany) for microbial

cultivation. The food waste hydrolysate was transferred to the anodic chamber of PV-S-MPEC.

2.9. Chemical oxygen demand analysis and performance analysis

Chemical oxygen demand was determined by Hach Method 8000. The COD digestion vials (testing range 20 to 1500 mg L^{-1} COD, HACH USA) with solution were used. The 2 mL diluted anolyte was transferred to the digestion vials and underwent digestion according to the method. The resulting solutions were analysed by UV-vis spectroscopy (Shimazu, UV3600).

3. Results and discussions

3.1. Characterization of *Shewanella oneidensis* MR-1 coated tungsten(VI) oxide (WO_3)

The WO_3 nanoplate photoelectrodes were fabricated on 1 cm × 2.5 cm glass substrates coated with fluorine-doped tin oxide (FTO), serving as the photoanode in a *Shewanella*-mediated photoelectrochemical cell (S-MPEC). These photoelectrodes were connected using titanium (Ti) wire (Fig. S1a†). High-magnification scanning electron microscopy (SEM) images were obtained for MR-1 coated carbon cloth (CC), MR-1 coated WO_3, and bare WO_3 (Fig. 1a–c). The morphology of bare WO_3 was consistent with previously reported structures.[42] The appearance of the WO_3 photoelectrode and the attachment of MR-1 biofilm after (bio) photoelectrochemical reaction were documented (Fig. S1b†). The dimensions of the WO_3 nanowires were significantly smaller than the bacteria, with an average length of 1 μm and 100 nm thick, as evident in the SEM images after the dehydration process (Fig. 1b and c). The X-ray diffraction (XRD) patterns of WO_3 and FTO were compared with the Joint Committee on Powder Diffraction Standards (JCPDS) Card File No. 33-0664 and 00-005-0467, confirming the presence of a nanowire arrayed WO_3 on the FTO substrate.

The optical properties of the WO_3 photoelectrodes were also investigated. The UV-vis absorption spectrum (Fig. S2a†) showed minimal changes in WO_3 before and after photoelectrochemical testing. However, the presence of MR-1 bacteria on WO_3 led to increased absorption between 500 nm and 700 nm, indicating biofilm formation on the photoelectrode surface. Meanwhile, the Tauc plot, a graphical representation derived from UV-vis absorption spectra, allows us to estimate the bandgap energy of semiconductors by extrapolating the linear portion of the $(\alpha h\nu)^2$ *vs.* $h\nu$ curve, where α is the absorption coefficient, and $h\nu$ is the photon energy. Also showed a reduction in bandgap from 2.84 eV to 2.5 eV after biofilm formation on the photoelectrode (Fig. S2b†). Photoluminescence (PL) characterization was

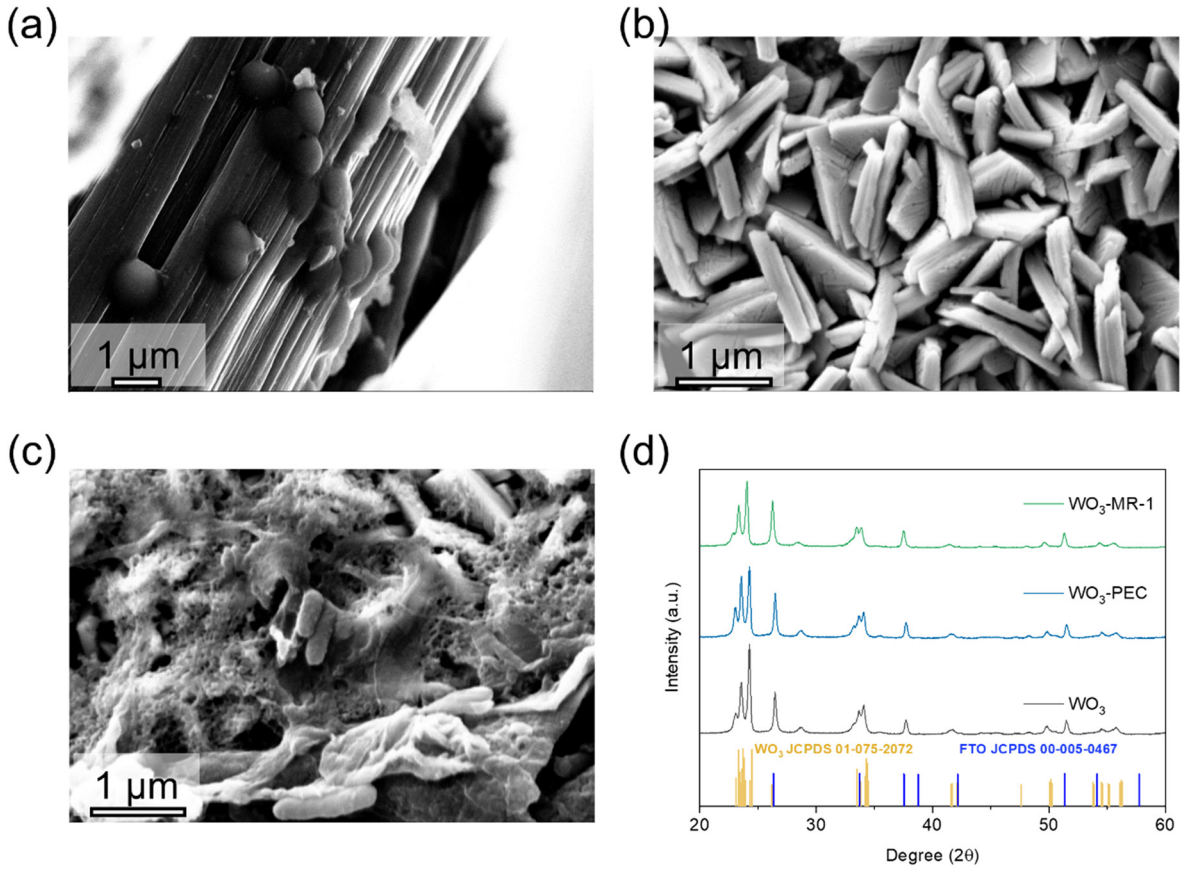

Fig. 1 SEM image of (a) carbon cloth (CC) with MR-1, (b) WO_3 and (c) WO_3 with MR-1. The white rectangular bar on the bottom left-hand corner of each graph indicates the dimensions with 1 μm. (d) XRD patterns of WO_3, WO_3 photoelectrode, and WO_3-MR-1 biophotoelectrode.

performed to further confirm the changes in the optical properties of WO_3 after (bio)photoelectrochemical reactions (Fig. S3a†). The results indicated no shift in the emission peaks at 468 nm post-reaction. The decrease in PL intensity can be attributed to electron transfers from WO_3 to impurities (in photoelectrochemical reaction) and MR-1 (in biophotoelectrochemical reaction). Fig. S3b† shows the time-resolved PL analysis. Bare WO_3 exhibits the highest average lifetime of 1.875 ns, indicating moderate recombination dynamics with significant surface recombination. In contrast, WO_3-PEC shows reduced recombination lifetimes compared to bare WO_3, suggesting improved recombination dynamics through reduced surface and bulk recombination. WO_3-MR-1 reveals the shortest lifetimes and the lowest average lifetime of 0.601 ns, indicating significantly enhanced recombination dynamics. MR-1 bacteria substantially reduces surface and bulk recombination, likely due to enhanced charge separation and transfer facilitated by the bacteria.

3.2. Photoelectrochemical characterization

The LSV for the WO_3 photoanode was performed to establish a baseline photoelectrochemical response without biological influence, focusing on the inherent material properties and light-induced electron dynamics. In contrast, LSV on the S-MPEC incorporated the biological components, specifically targeting the interactions between the WO_3 photoanode and the *Shewanella oneidensis* MR-1 biofilm. This comparative approach allowed us to directly assess the enhancement in photocurrent and electrochemical activity due to the synergistic effects of the semiconductor–bacteria interface. The WO_3 photoanode achieved a photocurrent density of 0.68 mA cm^{-2} at +0.2 V *vs.* Ag/AgCl 3.5 M KCl, corresponding to +1.23 V *vs.* RHE at pH 13.6. This performance is in agreement with established literature values. To mitigate photocurrent and overpotential losses, hydrogen peroxide (H_2O_2) was utilized as a sacrificial reducing agent. Subsequently, we enhanced the system by adding 100 mM H_2O_2 to a 1 M NaOH electrolyte. This modification increased the photocurrent to approximately 1.3 mA cm^{-2}, as shown in Fig. S4.† This improvement suggests the activation of surface species capable of hole trapping and enhancing water photo-oxidation on the WO_3 nanoplate.

In the solar-assisted microbial photoelectrochemical cell (S-MPEC) context, LSV experiments were carried out using the WO_3 photoelectrode as the working electrode, with a platinum wire as the counter electrode. The experiments were conducted at a scan rate of 10 mV s^{-1}, focusing on a potential window from −0.2 V to 1.0 V to elucidate the effects of illumination on the electrochemical interactions between WO_3 and MR-1. As depicted in Fig. 2a, the electrochemical activity was minimal under dark conditions, with the WO_3 photoelectrodes showing negligible current. However, under illuminated conditions, there was a significant enhancement in photocurrent density, aligning with findings reported in the literature. Interestingly, in the absence of light, the presence of *S. oneidensis* cells contributed to a notable increase in current density. The dark current density observed with the WO_3-MR-1 biophotoelectrode reached 0.826 A m^{-2}, which was considerably higher than the 0.289 A m^{-2} recorded for the bare WO_3 photoelectrode at 0.8 V. This increase indicates that under an external bias, the high interfacial energy barrier typically associated with the WO_3 electrode is effectively surpassed, facilitating the transfer of bioelectrons from MR-1 cells to the WO_3 anode and into the external circuit.

Additionally, Fig. 2a illustrates that the photocurrent of the bare WO_3 photoelectrode reached 2.97 A m^{-2} at 0.8 V, which was significantly higher than the 0.749 A m^{-2} observed at the same potential for the WO_3-MR-1 biophotoelectrode. The power density of the microbial electrochemical cell (MEC) with the CC-MR-1 bioelectrode was recorded at 0.680 W m^{-2}. Under visible light illumination, the power densities for the bare WO_3 and WO_3-MR-1 photoelectrodes were 0.599 W m^{-2} and 2.375 W m^{-2}, respectively. These findings indicate that the efficiency of substrate utilization by the exoelectrogenic bacteria MR-1 substantially enhances the performance of the S-MPEC system, regardless of the lighting conditions. This suggests that the intrinsic resistance of the WO_3 photoelectrode can be effectively mitigated by applying an external bias. Under solar illumination, photoexcited holes in the valence band of the photoanodes potentially recombine with bioelectrons from MR-1, which transforms the substrate into bioelectrons, thereby increasing the photocurrent density and promoting greater electron flow to the cathode *via* the external circuit.

Additionally, cyclic voltammetry provided further insights into the reversible and irreversible processes occurring at the electrode surfaces, showing a distinguish between the electrochemical behaviors of the WO_3 photoanode in the absence and presence of the biofilm. The CV experiments involved a series of working electrodes—CC-MR-1, bare WO_3, and WO_3-MR-1—with Ag/AgCl (3.5 M KCl) as the reference electrode and platinum (Pt) as the counter electrode. CV scans were performed in LB medium supplemented with 10 μM riboflavin, spanning a potential range from −1.0 V to +0.2 V *versus* SCE for the CC-MR-1, WO_3, and WO_3-MR-1 electrodes. For the CC-MR-1 electrode, cathodic and anodic peak potentials (E_{pc} and E_{pa}) were observed at −0.441 V and −0.098 V *versus* Ag/AgCl, respectively. Similarly, for the WO_3-MR-1 electrode, E_{pc} and E_{pa} were −0.301 V *versus* Ag/AgCl and −0.158 V *versus* Ag/AgCl, respectively. The midpoint potentials (E_0), calculated as $E_0 = (E_{pc} + E_{pa})/2$, were −0.230 V for WO_3-MR-1 and −0.270 V for CC-MR-1. These results correlate with the well-defined redox potentials of c-type cytochromes, which have a midpoint potential of around −0.410 V *versus* Ag/AgCl. The shuttle-mediated catalytic potential matches previous findings.[43–45] Our experimental analysis confirms that the interaction between MR-1 electrocigens and WO_3 involves

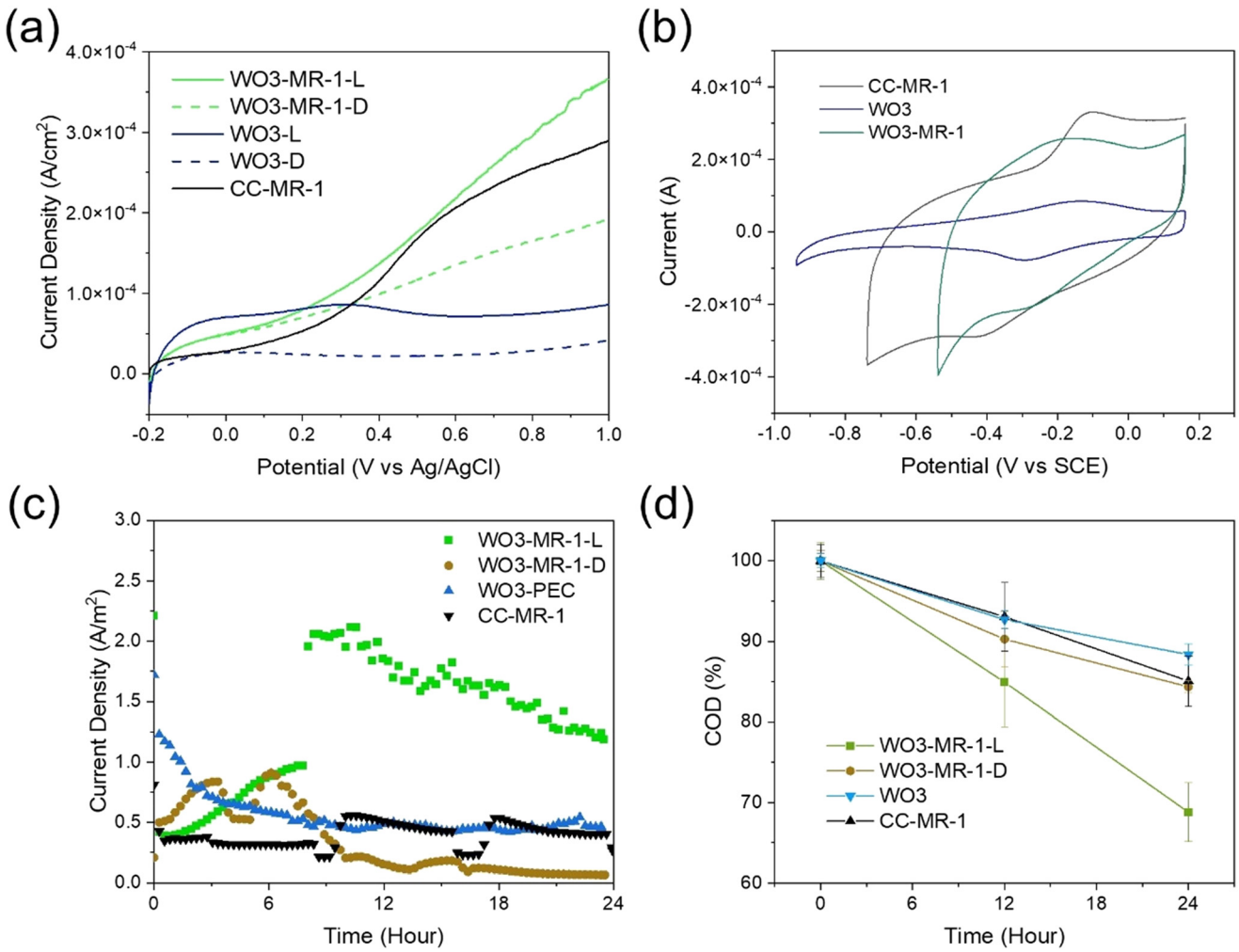

Fig. 2 (a) LSV, (b) CV, and (c) *i–t* curve under external bias of 0.8 V of S-MPEC using CC-MR-1, WO_3, and WO_3-MR-1 as anode under dark and light conditions. (d) Record of COD in the percentage of S-MPEC using CC-MR-1, WO_3, and WO_3-MR-1 as an anode.

c-type cytochromes, facilitating extracellular electron transfer.

The long-term stability of the solar-assisted microbial photoelectrochemical cell (S-MPEC) system was evaluated using current–time (*i–t*) measurements over 24 hours. The test was conducted and a bias voltage of 0.8 V *vs.* Ag/AgCl. The current–time response for various experimental setups is illustrated in Fig. 2c. For the WO_3-MR-1 biophotoelectrode under illumination, an initial increase in current density was observed from 0 to 3 hours, followed by a decline from 6 to 8 hours. This pattern suggests the ongoing formation and possibly the self-regulation of the biofilm on the WO_3 photoelectrode under the combined influence of irradiation and electrical bias. In contrast, under irradiated conditions, the photocurrent density of the WO_3-MR1 electrode not only increased but sustained higher levels for up to 8 hours, indicating more robust biofilm activity and electron transfer processes. Comparatively, the current density in the WO_3-MR-1 setup was fourfold higher than that of the bare WO_3 under similar irradiated conditions and four times greater than that observed in the CC-MR-1 under dark conditions. These results underscore the enhanced durability and electrochemical efficiency of the MR-1 when interfaced with WO_3 in the photoelectrochemical system.

To understand the relationship between bioelectron production and the operation of S-MPEC, the chemical oxygen demand (COD) was monitored at 12-hour intervals, as shown in Fig. 2d. The COD reduction exhibited a rapid decline during the initial 12 hours, aligning with the active growth phase of the microbial cells.[42] The initial COD was approximately 13 000 mg L^{-1}, as detailed in Table S1.† After 24 hours, the COD for the CC-MR-1 setup decreased from 12 490 mg L^{-1} to 10 623 mg L^{-1}, which corresponds to a removal rate of 1811 mg L^{-1} per day. For the WO_3-MR-1 configuration, the COD reduced from 13 207 mg L^{-1} to 11 140 mg L^{-1}, achieving a notable removal rate of 3867 mg L^{-1} per day.

These findings demonstrate that the WO_3-MR-1 setup enhances the photocurrent density and significantly improves the COD consumption rate under irradiated conditions. This suggests that photoexcited holes in the WO_3

contribute effectively to the oxidation processes, thereby driving the efficient electron transfer from MR-1.

3.3. Extracellular electron transfer kinetics

Cyclic voltammetry was conducted at different scan rates to investigate the heterogeneous electron transfer kinetics of different electrodes. To facilitate the analysis, 10 μM Riboflavin was added to each electrode system, serving as a redox shuttle. This addition enables the observation of shuttle-mediated catalytic currents and provides insights into the electron transfer kinetics at the electrode|electrolyte interfaces for the CC-MR-1, WO_3, and WO_3-MR-1. In Fig. 3a, c, and e, significant peak broadening and peak

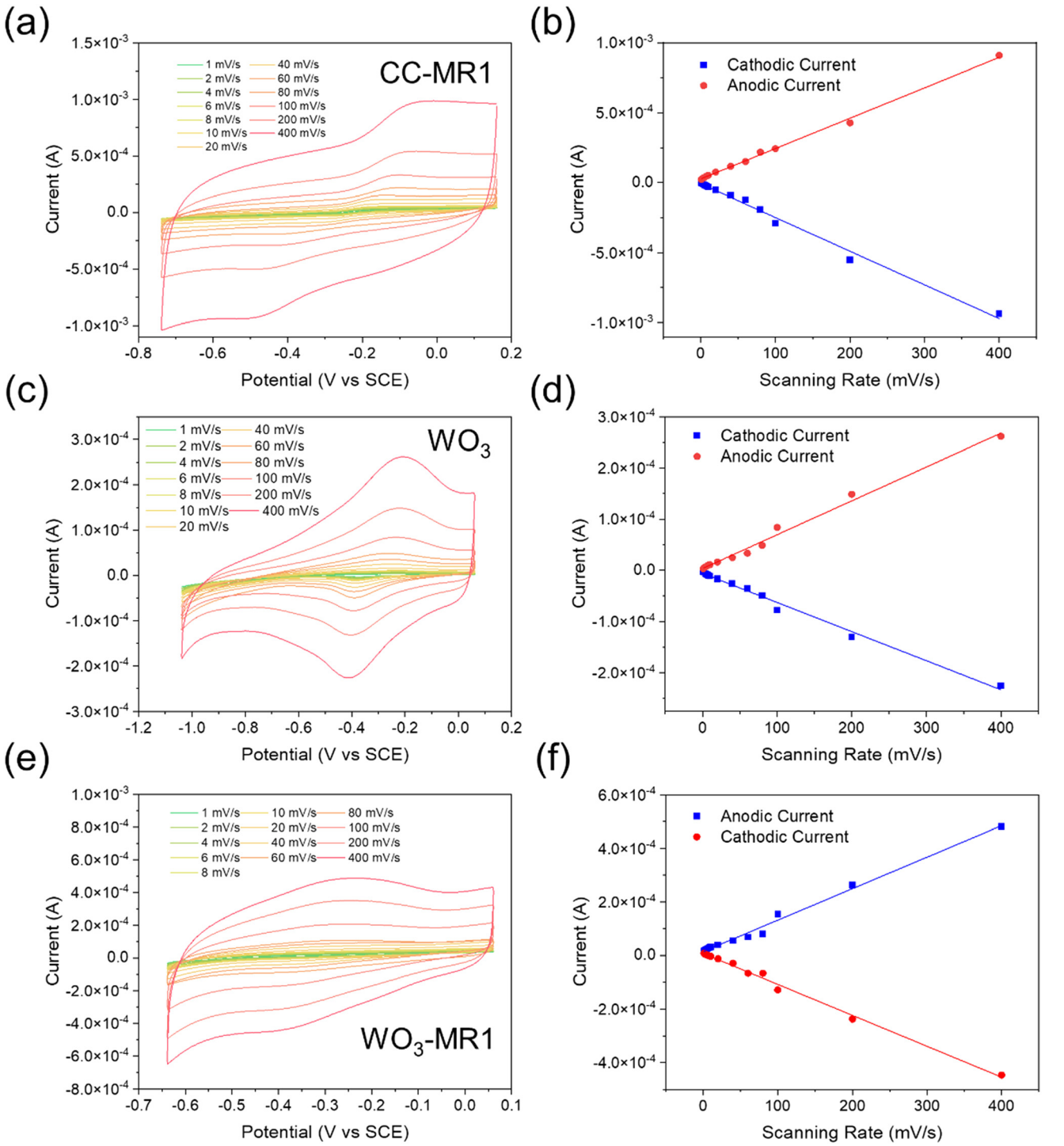

Fig. 3 CV at different scan rates from 1 mV s^{-1} to 40 mV s^{-1} of (a) CC-MR-1, (c) WO_3, and (e) WO_3-MR-1; peak current *vs.* scan rate plot of (b) CC-MR-1, (d) WO_3 and (f) WO_3-MR-1.

separation were observed in the CV profiles, indicating the redox processes associated with the immobilized flavin.[46,47] Additionally, a peak shift of approximately 0.1 V *vs.* SCE was noted, which is attributed to the internal resistance of the semiconductor electrode, specifically WO_3 in this case. The relationship between peak current densities and different scanning rates was analyzed to further elucidate the redox species' nature within the MR-1 biofilm. As shown in Fig. 3b, the peak currents were linearly related to the scanning rates, with a correlation coefficient (R^2) 0.99. This linearity suggests the presence of a diffusion regime oriented perpendicular to the electrode surface. The Randles–Sevcik equation (eqn (1)) can be employed to describe this behavior.

$$I_{rev} = (2.69 \times 10^5) n^{3/2} A C D^{1/2} v^{1/2} \quad (1)$$

The Tafel plot in Fig. S7† was obtained from the descending parts of the cathodic and ascending parts of anodic peaks of the cyclic voltammogram. We then determined α using the slope of the plot of log(i) *versus* potential, as shown in eqn (2).[48]

$$\text{Slope} = \frac{\alpha F}{2.3RT} \text{ or } \frac{-\alpha F}{2.3RT} \quad (2)$$

To quantify the heterogeneous electron-transfer rate constant (k_0), the Gileadi method was employed. This method is instrumental in determining the critical scan rate (V_c) where the electrochemical reaction transitions from reversible to irreversible or from quasi-reversible to irreversible. This transition point is crucial for understanding the electron transfer processes' kinetics and the electrode–electrolyte interface's dynamic behavior.[49] The V_c was graphically evaluated by plotting E_p against the log of scan rate at low and high scan rates (Fig. S6†). The graphical representation typically results in two distinct linear segments corresponding to the lower and higher scan rate domains. Two different slopes are obtained by fitting lines to these segments, reflecting the different kinetic regimes at varied scan rates. The intersection of the two lines provided the V_c, and k^0 was determined by eqn (3).[50]

$$\log k^0 = -0.48\alpha + 0.52 + \log\left(\frac{nF\alpha V_c D}{2.303RT}\right)^{\frac{1}{2}} \quad (3)$$

As detailed in Table 1, the electrochemical characterization of the WO_3-MR-1 electrode shows diffusion coefficients for the reduction and oxidation reactions at 1.66×10^{-8} cm^2 s^{-1} and 2.29×10^{-8} cm^2 s^{-1}, respectively. These values are accompanied by high electron-transfer rate constants of 8.02×10^{-5} cm s^{-1} for reduction and 9.02×10^{-5} cm s^{-1} for oxidation. The diffusion coefficients and rate constants for the CC-MR-1 electrode and the bare WO_3 photoelectrode are also provided for comparative purposes. The WO_3-MR-1 electrode demonstrates a higher diffusion coefficient and faster rate constant than the bare WO_3 photoelectrode. This indicates more efficient electron transfer processes at the solid–liquid interface in the WO_3-MR-1 system. Such superior electrochemical properties underscore the potential of WO_3-MR-1 as a highly promising candidate for bio-photoelectrochemical applications. The enhanced performance of WO_3-MR-1 can be attributed to the synergistic interaction between the microbial biofilm and the semiconductor material, which facilitates a more efficient heterogeneous electron transfer.

3.4. Electrochemical impedance spectroscopy (EIS)

We conducted electrochemical impedance spectroscopy (EIS) to assess the charge transfer resistance within the photoelectrochemical cell. The Nyquist plots derived from EIS for three different electrodes (CC-MR-1, WO_3, and WO_3-MR-1) were analyzed to assess the electrochemical behavior of both control and experimental reactors, as shown in Fig. 4. The high-frequency intercept with the x-axis in these plots indicates the ohmic resistance of the cell, which includes contributions from the inherent resistances of the electrolyte, electrodes, and interface contacts. The Nyquist arc's magnitude reflects the total resistance encompassing these components. An appropriate equivalent circuit model, depicted in Fig. 4a, was employed to interpret the EIS data. This model quantifies various resistance components such as charge transfer resistance, mass transfer resistance, and ohmic resistance within the solar-assisted microbial photoelectrochemical cell (S-MPEC) system.[51] The values for different circuit elements, which were fitted to this model, are provided in Table S3.† From the analysis, the electrolyte resistance (R_s) observed was highest for the carbon cloth electrode at 38.4 Ω. It was lower for the bare WO_3 electrode at 13.72 Ω, and the lowest for the WO_3-MR-1 electrode at 8.637 Ω. This decrease in resistance with the incorporation of MR-1 bacteria into the WO_3 electrode suggests an enhancement in ionic conductivity, likely facilitated by the biological activity of the bacteria. Furthermore, the Nyquist

Table 1 The kinetic parameters of CC-MR-1, WO_3, and WO_3-MR-1, including $E°$, D, $k°$, and α in LB-M9 solution with 10 μM riboflavin at room temperature

	CC-MR-1		WO_3		WO_3-MR-1	
	Reduction	Oxidation	Reduction	Oxidation	Reduction	Oxidation
$E°$ (V *vs.* SCE)	−0.472	−0.375	−0.280	−0.151	−0.259	−0.180
10^{-8} D (cm^2 s^{-1})	2.91	0.356	0.2	0.24	1.66	2.29
α	0.075	0.13	0.111	0.087	0.138	0.112
10^{-6} $k°$ (cm s^{-1})	78.8	36.5	21.1	29.4	80.2	90.2

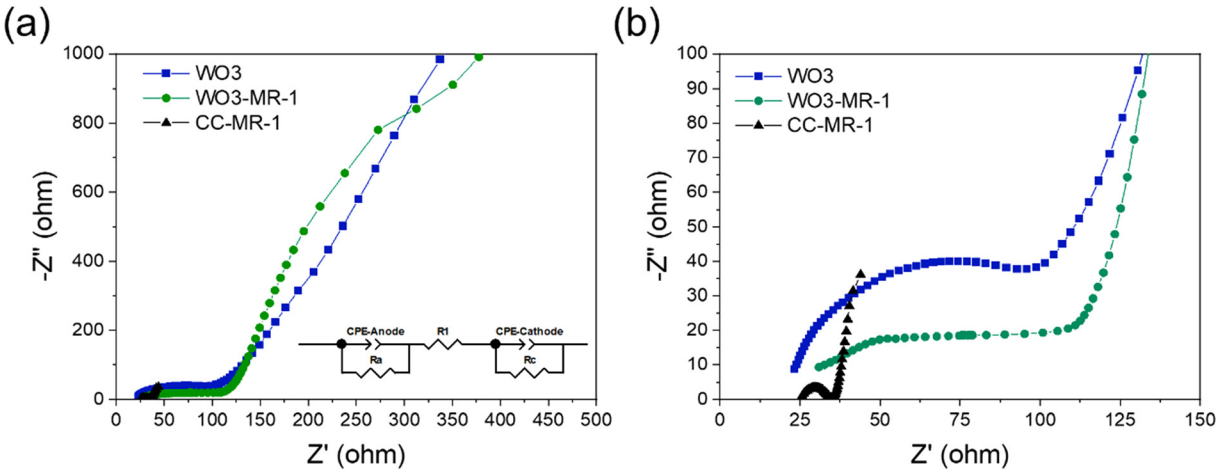

Fig. 4 (a) Electrochemical impedance plots of electrodes of CC-MR-1, WO_3 and WO_3-MR-1 with an equivalent circuit model used to fit experimental data; (b) enlarged electrochemical impedance plots of (a).

plots revealed that the anode resistance was significantly higher for the bare WO_3 (4373 Ω) and even more so for the WO_3-MR-1 (4901 Ω) compared to the carbon cloth (1007 Ω). This increase in anode resistance with the introduction of MR-1 onto the WO_3 electrode points to potential complications in electron transfer efficiency at the anode. Regarding cathodic reactions, the cathodic charge-transfer resistance for the WO_3-MR-1 (39.9 Ω) and CC (5.28 Ω) was found to be lower than that of bare WO_3 (82.1 Ω), highlighting a limitation in the cathodic charge transfer capabilities of the bare WO_3 electrode. This suggests that MR-1 bacteria facilitates a more efficient transfer of H+ ions from the oxidation reaction in the anodic chamber, improving overall charge transfer at the cathode.[52]

3.5. Mechanistic insight into electricity generation in S-MPEC

Based on the findings from this study, we have developed a model to explain the current generation mechanism in the solar-assisted microbial photoelectrochemical cell (S-MPEC) utilizing a WO_3 nanoplate photoelectrode and *S. oneidensis*, as illustrated in Fig. 5. The observation that the system produces only a minimal current in the absence of light suggests that the polarization resistance at the WO_3 nanoplate electrode may hinder the transfer of bioelectrons. These electrons originate from the exoelectrogens and travel through the conduction band of the WO_3 nanoplate to the FTO substrate, a process that appears to be impeded under dark conditions.[15,53] Under illuminated conditions, however, the separation of photogenerated electron–hole pairs is significantly enhanced. This improvement is primarily due to the recombination of bioelectrons—derived from lactate/pyruvate (−0.185 V) transferred by the outer membrane c-type cytochromes (OM c-Cyts) of *S. oneidensis* (approximately −0.110 V *vs.* Ag/AgCl)—with the photoexcited holes (2.86 eV *vs.* NHE) on the surface of the WO_3 nanoplate photoelectrodes. This recombination process effectively leads to a higher current output.[54,55]

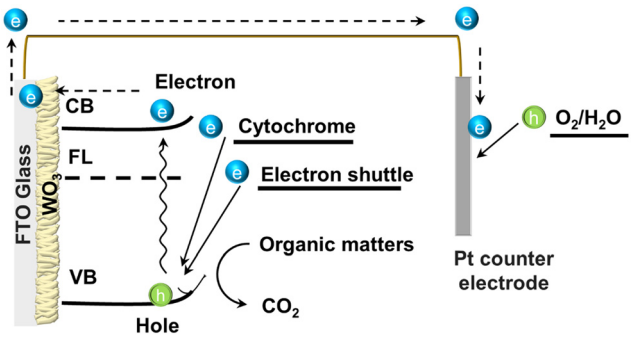

Fig. 5 Schematic diagram of the photocurrent generation by the WO_3 electrode with MR-1 bacteria. FL, CB, and VB represent the fermi level, conduction, and valence bands, respectively.

3.6. PV-S-MPEC system

To enhance the performance of the solar-assisted microbial photoelectrochemical cell (S-MPEC), a commercially available silicon photovoltaic (PV) module delivering 3.5 V was integrated into the system. The performance of this setup is shown in Fig. S5a and b,† where the voltage over time and the associated current and power densities were derived using the eqn (4) and (5):

$$\text{Voltage } (V) = \text{Current } (I) \times \text{Resistance } (R) \quad (4)$$

$$\text{Power } (P) = \text{Current } (I) \times \text{Voltage } (V) \quad (5)$$

EIS determined the overall resistances for systems employing WO_3 and CC bioanodes to be 4949.5 Ω and 345.65 Ω, respectively. S-MPEC with the CC bioanode, the output voltage of SiPV decreased to 3.29 V, yielding a current density of 1.40 A m^{-2} and a power density of 4.62 W m^{-2}. In contrast, the S-MPEC using a WO_3 bioanode showed a voltage

drop to 3.28 V but achieved a higher current density of 6.70 A m^{-2} and a power density of 21.99 W m^{-2}. The resulting power density of PV-S-MPEC outperforms the reported value of 0.75 W m^{-2} of a microbial fuel cell with polycrystalline silicon solar cell integrated system.[17]

Chemical oxygen demand (COD) was also monitored to assess the organic matter reduction efficiency. Initially set at approximately 10 000 mg L^{-1}, the COD in the PV-S-MPEC using CC-MR-1 bioanode decreased from 10 090 mg L^{-1} to 5590 mg L^{-1} over 24 hours, corresponding to a removal rate of 4500 mg L^{-1} per day. The PV-S-MPEC using WO_3-MR-1 bioanode displayed a more substantial reduction, from 10 257 mg L^{-1} to 2090 mg L^{-1}, presenting a removal rate of 8167 mg L^{-1} per day. Based on the calculation (ESI†), the food waste removal rate of PV-S-MPEC using CC-MR-1 bioanode and WO_3-MR-1 bioanode was estimated to be 83.67 g per day. The PV-S-MPEC system demonstrated a remarkable improvement in output power density and COD removal rate, showing the effectiveness of PV integration in boosting the system's overall efficiency and stability.

4. Conclusion

This study explores the bio-photoelectrochemical interactions between tungsten(VI) oxide and *Shewanella oneidensis* MR-1 within hybrid bio-photoelectrochemical devices. These hybrid systems demonstrate significantly improved photoelectrochemical performance when incorporating live cells. Linear sweep voltammetry reveals that WO_3 photoelectrodes in the solar-assisted microbial photoelectrochemical cell (S-MPEC) exhibits a remarkable 400% increase in current density compared to an abiotic medium under a 0.80 V external bias. Electrochemical impedance spectroscopy (EIS) analysis indicates that the overall resistance of the S-MPEC system using a WO_3 anode is considerably higher than that with a carbon cloth anode. This suggests that the presence of MR-1 bacteria reduces solution resistance and enhances ionic conductivity. Additionally, the cathodic charge-transfer resistance for the WO_3-MR-1 is lower than that for bare WO_3, indicating a more efficient electrochemical interaction facilitated by the bacteria. In the PV-S-MPEC system employing WO_3 as the photoanode, the output voltage is measured at 3.28 V, corresponding current density and power density of 6.70 A m^{-2} and 21.99 W m^{-2}, respectively. This study demonstrates that integrating photovoltaic modules with microbial photoelectrochemical cells provides a robust framework that enhances bioelectrochemical performance and waste degradation. Furthermore, the WO_3-MR-1 system demonstrated the most efficient COD removal rate under irradiation, achieving a rate of 8167 mg L^{-1} per day, compared to 4500 mg L^{-1} per day for the CC-MR-1 system. This efficiency underscores the role of photoexcited holes in driving the oxidation reactions of the MR-1 species, thereby enhancing the bioelectrochemical performance. These findings not only pave the way for new directions in the development of practical S-MPEC systems but also provide crucial insights into the mechanisms of electron transfer and energy conversion within these systems, as well as the natural synergy between sunlight, semiconductors, and electricigens.

Data availability

Data available on request from the authors.

Conflicts of interest

There are no conflicts to declare.

Note added after first publication

This article replaces the version published on 1st October 2024, which contained errors in the caption for Fig. 1 as well as use of the incorrect valency for compound 'tungsten(IV) oxide' throughout and this has been corrected to 'tungsten(VI) oxide' in this version.

Acknowledgements

The authors acknowledge financial support from the Research Grants Council of Hong Kong (grant no. CityU 21203518 and F-CityU106/18), Innovation and Technology Commission (grant no. MHP/104/21), Shenzhen Science Technology and Innovation Commission (grant no. JCYJ20210324125612035, R-IND12303 and R-IND12304), City University of Hong Kong (grant no. 9229160, 9360140, 7005289, 7005580, 7005720, 9667213, 9667229, 9680331 and 9678291), Australian Research Council (ARC) Discovery Early Career Researcher Award (grant no. DE160100589), National Natural Science Foundation of China (grant no. 21974131), and C. H. Mak thanks for the financial support from the Hong Kong Jockey Club under the research work Hong Kong JC STEM Lab for Circular Bio-economy (Project No. 2023-0078).

References

1 S. Liu, Y. Jin, S. Huang, Q. Zhu, S. Shao and J. C.-H. Lam, One-pot redox cascade paired electrosynthesis of gamma-butyrolactone from furoic acid, *Nat. Commun.*, 2024, **15**(1), 1141.

2 C. A. Richard, Z. Pan, H.-Y. Hsu, S. Cekli, K. S. Schanze and J. R. Reynolds, Effect of Isomerism and Chain Length on Electronic Structure, Photophysics, and Sensitizer Efficiency in Quadrupolar (Donor) 2–Acceptor Systems for Application in Dye-Sensitized Solar Cells, *ACS Appl. Mater. Interfaces*, 2014, **6**(7), 5221–5227.

3 L. Fu, K. Fu, X. Gao, S. Dong, B. Zhang, S. Fu, H.-Y. Hsu and G. Zou, Enhanced Near-Infrared Electrochemiluminescence from Trinary Ag–In–S to Multinary Ag–Ga–In–S Nanocrystals via Doping-in-Growth and Its Immunosensing Applications, *Anal. Chem.*, 2021, **93**(4), 2160–2165, DOI: **10.1021/acs.analchem.0c03975**.

4 X. Fu, T. He, S. Zhang, X. Lei, Y. Jiang, D. Wang, P. Sun, D. Zhao, H.-Y. Hsu and X. Li, Halogen-halogen bonds enable improved long-term operational stability of mixed-halide perovskite photovoltaics, *Chem*, 2021, **7**(11), 3131–3143.

5 Q. Zhu, B. Gong, S. Huang, Y. Jin, S. Liu, S. Shao, Y. Yang, T. Cataldo, N. M. Bedford and J. C.-H. Lam, Rhombohedral ZnIn 2 S 4-catalysed anodic direct electrochemical oxidative cleavage of C–O bond in α-O-4 linkages in ambient conditions, *Green Chem.*, 2024, **26**(7), 4135–4150.

6 K. L. Ong, G. Kaur, N. Pensupa, K. Uisan and C. S. K. Lin, Trends in food waste valorization for the production of chemicals, materials and fuels: Case study South and Southeast Asia, *Bioresour. Technol.*, 2018, **248**, 100–112.

7 T. N. D. Cao, T. Wang, Y. Peng, H.-Y. Hsu, H. Mukhtar and C.-P. Yu, Photo-assisted microbial fuel cell systems: critical review of scientific rationale and recent advances in system development, *Crit. Rev. Biotechnol.*, 2024, **44**(1), 31–46.

8 S. Huang, Y. Jin, M. Zhang, K. Yan, S.-P. Feng and J. C.-H. Lam, MoS 2-catalyzed selective electrocatalytic hydrogenation of aromatic aldehydes in an aqueous environment, *Green Chem.*, 2022, **24**(20), 7974–7987.

9 S. Rao, X. Zou, S. Wang, T. Shi, Y. Lu, L. Ji, H.-Y. Hsu, Q. Xu and X. Lu, Electrodeposition of porous Sn-Ni-Cu alloy anode for lithium-ion batteries from nickel matte in deep eutectic solvents, *J. Electrochem. Soc.*, 2019, **166**(10), D427.

10 S. Javaid, X. Xu, W. Chen, J. Chen, H.-Y. Hsu, S. Wang, X. Yang, Y. Li, Z. Shao and F. Jones, *et al.* Ni2+/Co2+ doped Au-Fe7S8 nanoplatelets with exceptionally high oxygen evolution reaction activity, *Nano Energy*, 2021, **89**, 106463, DOI: **10.1016/j.nanoen.2021.106463**.

11 S. P. Santoso, S.-P. Lin, T.-Y. Wang, Y. Ting, C.-W. Hsieh, R.-C. Yu, A. E. Angkawijaya, F. E. Soetaredjo, H.-Y. Hsu and K.-C. Cheng, Atmospheric cold plasma-assisted pineapple peel waste hydrolysate detoxification for the production of bacterial cellulose, *Int. J. Biol. Macromol.*, 2021, **175**, 526–534, DOI: **10.1016/j.ijbiomac.2021.01.169**.

12 C. Wang, K. Liu, Y. Jin, S. Huang and J. Chun-Ho Lam, Amorphous RuO2 Catalyst for Medium Size Carboxylic Acid to Alkane Dimer Selective Kolbe Electrolysis in an Aqueous Environment, *ChemSusChem*, 2023, **16**(16), e202300222.

13 F. Qian, H. Wang, Y. Ling, G. Wang, M. P. Thelen and Y. Li, Photoenhanced electrochemical interaction between Shewanella and a hematite nanowire photoanode, *Nano Lett.*, 2014, **14**(6), 3688–3693.

14 H. Y. Chung, R. J. Wong, R. Amal and Y. H. Ng, Engineering the interfacial contact between Bi2WO6 and WO3 heterojunction photoanode for improved charge transportation, *Energy Fuels*, 2022, **36**(19), 11550–11558.

15 J. Cao, Y. Shi, J. Xin, S. Kong and X. Wang, Application of microbial fuel cells with tungsten-based semiconductor modified electrode in the treatment of Cr (VI) pollutions, *Biochem. Eng. J.*, 2023, **198**, 109034.

16 H. Ding, Y. Li, A. Lu, X. Wang and C. Wang, Promotion of anodic electron transfer in a microbial fuel cell combined with a silicon solar cell, *J. Power Sources*, 2014, **253**, 177–180.

17 Z. Sun, R. Cao, M. Huang, P. Sun, C. Tang and D. Chen, Enhanced electricity generation and pollutant removal in a microbial fuel cell combined with a solar cell, *J. Renewable Sustainable Energy*, 2015, **7**(4), 043109.

18 K.-J. Chae, M.-J. Choi, K.-Y. Kim, F. F. Ajayi, I.-S. Chang and I. S. Kim, A solar-powered microbial electrolysis cell with a platinum catalyst-free cathode to produce hydrogen, *Environ. Sci. Technol.*, 2009, **43**(24), 9525–9530.

19 C.-N. Wu, L.-C. Sun, Y.-L. Chu, R.-C. Yu, C.-W. Hsieh, H.-Y. Hsu, F.-C. Hsu and K.-C. Cheng, Bioactive compounds with anti-oxidative and anti-inflammatory activities of hop extracts, *Food Chem.*, 2020, **330**, 127244.

20 A. Andreas, Z. G. Winata, S. P. Santoso, A. E. Angkawijaya, M. Yuliana, F. E. Soetaredjo, S. Ismadji, H.-Y. Hsu, A. W. Go and Y.-H. Ju, Biocomposite hydrogel beads from glutaraldehyde-crosslinked phytochemicals in alginate for effective removal of methylene blue, *J. Mol. Liq.*, 2021, **329**, 115579, DOI: **10.1016/j.molliq.2021.115579**.

21 X. Yang, J. Yang, M. I. Ullah, Y. Xia, G. Liang, S. Wang, J. Zhang, H.-Y. Hsu, H. Song and J. Tang, Enhanced Passivation and Carrier Collection in Ink-Processed PbS Quantum Dot Solar Cells via a Supplementary Ligand Strategy, *ACS Appl. Mater. Interfaces*, 2020, **12**(37), 42217–42225, DOI: **10.1021/acsami.0c08135**.

22 F. F. Ajayi, K.-Y. Kim, K.-J. Chae, M.-J. Choi, S.-Y. Kim, I.-S. Chang and I. S. Kim, Study of hydrogen production in light assisted microbial electrolysis cell operated with dye sensitized solar cell, *Int. J. Hydrogen Energy*, 2009, **34**(23), 9297–9304.

23 Q. Zeng, J. Li, J. Bai, X. Li, L. Xia and B. Zhou, Preparation of vertically aligned WO3 nanoplate array films based on peroxotungstate reduction reaction and their excellent photoelectrocatalytic performance, *Appl. Catal., B*, 2017, **202**, 388–396.

24 S. Rao, X. Zou, S. Wang, Y. Lu, T. Shi, H.-Y. Hsu, Q. Xu and X. Lu, Electrodeposition of Ni-Cu alloy films from nickel matte in deep eutectic solvent, *Mater. Chem. Phys.*, 2019, **232**, 6–15.

25 C. H. Mak, Y. Peng, M. H. Chong, L. Yu, M. Du, L. Ji, X. Zou, G. Zou, H.-H. Shen and S. P. Santoso, Photoenhanced interfacial electron transfer of a dual functional hematite biophotoelectrode, *J. Mater. Chem. C*, 2023, **11**(33), 11303–11311.

26 C.-C. Chang, Y.-C. Chen and C.-P. Yu, Microbial community dynamics in electroactive biofilms across time under different applied anode potentials, *Sustainable Environ. Res.*, 2022, **32**(1), 1–11.

27 R. Liu, C. H. Mak, X. Han, Y. Tang, G. Jia, K.-C. Cheng, H. Qi, X. Zou, G. Zou and H.-Y. Hsu, Efficient electronic coupling and heterogeneous charge transport of zero-dimensional Cs4PbBr6 perovskite emitters, *J. Mater. Chem. A*, 2020, **8**(45), 23803–23811, DOI: **10.1039/D0TA06076C**.

28 C. H. Mak, R. Liu, X. Han, Y. Tang, X. Zou, H. H. Shen, Y. Meng, G. Zou and H. Y. Hsu, Thermally Activated Delayed Phosphorescence and Interchromophore Exciton Coupling in a Platinum-Based Organometallic Emitter, *Adv. Opt. Mater.*, 2020, **8**(20), 2001023.

29 Y. Tang, C. H. Mak, R. Liu, Z. Wang, L. Ji, H. Song, C. Tan, F. Barrière and H. Y. Hsu, In Situ Formation of Bismuth-Based Perovskite Heterostructures for High-Performance Cocatalyst-Free Photocatalytic Hydrogen Evolution, *Adv. Funct. Mater.*, 2020, 2006919.

30 Y. Tang, C. H. Mak, J. Zhang, G. Jia, K.-C. Cheng, H. Song, M. Yuan, S. Zhao, J.-J. Kai and J. C. Colmenares, *et al.* Unravelling the Interfacial Dynamics of Bandgap Funneling in Bismuth-Based Halide Perovskites, *Adv. Mater.*, 2023, **35**(2), 2207835, DOI: **10.1002/adma.202207835**.

31 Y. Tang, C. H. Mak, C. Wang, Y. Fu, F.-F. Li, G. Jia, C.-W. Hsieh, H.-H. Shen, J. C. Colmenares and H. Song, *et al.* Bandgap Funneling in Bismuth-Based Hybrid Perovskite Photocatalyst with Efficient Visible-Light-Driven Hydrogen Evolution, *Small Methods*, 2022, **6**(8), 2200326, DOI: **10.1002/smtd.202200326**.

32 F. Meng, Y. Jia, J. Wang, X. Huang, Z. Gui, L. Huang, R. Li, R. Chen, J. Xu and W. Chen, *et al.* Dopant-Free Hole Transporting Molecules for Highly Efficient Perovskite Photovoltaic with Strong Interfacial Interaction, *Sol. RRL*, 2019, **3**(12), 1900319, DOI: **10.1002/solr.201900319**.

33 H.-Y. Hsu, H.-H. Hsieh, H.-Y. Tuan and J.-L. Hwang, Oxidized low density polyethylene: A potential cost-effective, stable, and recyclable polymeric encapsulant for photovoltaic modules, *Sol. Energy Mater. Sol. Cells*, 2010, **94**(6), 955–959.

34 Y. Peng, C. H. Mak, J.-J. Kai, M. Du, L. Ji, M. Yuan, X. Zou, H.-H. Shen, S. P. Santoso and J. C. Colmenares, *et al.* Recent progress on post-synthetic treatments of photoelectrodes for photoelectrochemical water splitting, *J. Mater. Chem. A*, 2021, **9**(47), 26628–26649, DOI: **10.1039/D1TA05935A**.

35 Z. Chen, H.-Y. Hsu, M. Arca and K. S. Schanze, Triplet Energy Transport in Platinum-Acetylide Light Harvesting Arrays, *J. Phys. Chem. B*, 2015, **119**(24), 7198–7209, DOI: **10.1021/jp509130b**.

36 H.-Y. Hsu, L. Ji, C. Zhang, C. H. Mak, R. Liu, T. Wang, X. Zou, S.-Y. Leu and E. T. Yu, Ultra-stable 2D layered methylammonium cadmium trihalide perovskite photoelectrodes, *J. Mater. Chem. C*, 2018, **6**(43), 11552–11560, DOI: **10.1039/C8TC02153H**.

37 C. H. Mak, X. Huang, R. Liu, Y. Tang, X. Han, L. Ji, X. Zou, G. Zou and H.-Y. Hsu, Recent progress in surface modification and interfacial engineering for high-performance perovskite light-emitting diodes, *Nano Energy*, 2020, **73**, 104752, DOI: **10.1016/j.nanoen.2020.104752**.

38 H.-Y. Hsu, L. Ji, M. Du, J. Zhao, T. Y. Edward and A. J. Bard, Optimization of Lead-free Organic–inorganic Tin (II) Halide Perovskite Semiconductors by Scanning Electrochemical Microscopy, *Electrochim. Acta*, 2016, **220**, 205–210.

39 C. H. Mak, X. Han, M. Du, J.-J. Kai, K. F. Tsang, G. Jia, K.-C. Cheng, H.-H. Shen and H.-Y. Hsu, Heterogenization of homogeneous photocatalysts utilizing synthetic and natural support materials, *J. Mater. Chem. A*, 2021, **9**(8), 4454–4504, DOI: **10.1039/D0TA08334H**.

40 Y. Tang, C. H. Mak, G. Jia, K.-C. Cheng, J.-J. Kai, C.-W. Hsieh, F. Meng, W. Niu, F.-F. Li and H.-H. Shen, *et al.* Lead-free hybrid perovskite photocatalysts: surface engineering, charge-carrier behaviors, and solar-driven applications, *J. Mater. Chem. A*, 2022, **10**(23), 12296–12316, DOI: **10.1039/D2TA01170K**.

41 H. Wu, T. H. Tan, R. Liu, H.-Y. Hsu and Y. H. Ng, Selective Ethanol Oxidation to Acetaldehyde on Nanostructured Zeolitic Imidazolate Framework-8-Wrapped ZnO Photothermocatalyst Thin Films, *Sol. RRL*, 2021, **5**(6), 2000423, DOI: **10.1002/solr.202000423**.

42 G. Zhu, Y. Yang, J. Liu, F. Liu, A. Lu and W. He, Enhanced photocurrent production by the synergy of hematite nanowire-arrayed photoanode and bioengineered Shewanella oneidensis MR-1, *Biosens. Bioelectron.*, 2017, **94**, 227–234.

43 F. Zhang, S.-J. Yuan, W.-W. Li, J.-J. Chen, C.-C. Ko and H.-Q. Yu, WO3 nanorods-modified carbon electrode for sustained electron uptake from Shewanella oneidensis MR-1 with suppressed biofilm formation, *Electrochim. Acta*, 2015, **152**, 1–5.

44 E. Marsili, D. B. Baron, I. D. Shikhare, D. Coursolle, J. A. Gralnick and D. R. Bond, Shewanella secretes flavins that mediate extracellular electron transfer, *Proc. Natl. Acad. Sci. U. S. A.*, 2008, **105**(10), 3968–3973.

45 D. Baron, E. LaBelle, D. Coursolle, J. A. Gralnick and D. R. Bond, Electrochemical measurement of electron transfer kinetics by Shewanella oneidensis MR-1, *J. Biol. Chem.*, 2009, **284**(42), 28865–28873.

46 C. N. Durfor, B. A. Yenser and M. L. Bowers, Attachment of riboflavin derivatives to electrode surfaces, *J. Electroanal. Chem. Interfacial Electrochem.*, 1988, **244**(1), 287–300, DOI: **10.1016/0022-0728(88)80111-6**.

47 C. Sumathi, P. Muthukumaran, S. Radhakrishnan, G. Ravi and J. Wilson, Riboflavin detection by α-Fe2O3/MWCNT/AuNPs-based composite and a study of the interaction of riboflavin with DNA, *RSC Adv.*, 2015, **5**(23), 17888–17896, DOI: **10.1039/C4RA14762F**.

48 J. Wang, *Analytical Electrochemistry*, A John Willey and Sons. Inc., New York, 2000, pp. 81–84.

49 N. K. Bhatti, M. S. Subhani, A. Y. Khan, R. Qureshi and A. Rahman, Heterogeneous electron transfer rate constants of viologen at a platinum disk electrode, *Turk. J. Chem.*, 2006, **29**(6), 659–668.

50 N. K. Bhatti, M. S. Subhani, A. Y. Khan, R. Qureshi and A. Rahman, Heterogeneous electron transfer rate constants of viologen monocations at a platinum disk electrode, *Turk. J. Chem.*, 2006, **30**(2), 165–180.

51 Z. He and F. Mansfeld, Exploring the use of electrochemical impedance spectroscopy (EIS) in microbial fuel cell studies, *Energy Environ. Sci.*, 2009, **2**(2), 215–219, DOI: **10.1039/B814914C**.

52 Z. He, Y. Huang, A. K. Manohar and F. Mansfeld, Effect of electrolyte pH on the rate of the anodic and cathodic reactions in an air-cathode microbial fuel cell, *Bioelectrochemistry*, 2008, **74**(1), 78–82, DOI: **10.1016/j.bioelechem.2008.07.007**.

53 S.-J. Yuan, H. He, G.-P. Sheng, J.-J. Chen, Z.-H. Tong, Y.-Y. Cheng, W.-W. Li, Z.-Q. Lin, F. Zhang and H.-Q. Yu, A photometric high-throughput method for identification of electrochemically active bacteria using a WO3 nanocluster probe, *Sci. Rep.*, 2013, **3**(1), 1315.

54 Y.-J. Chen and L.-Y. Chen, The study of carrier transfer mechanism for nanostructural hematite photoanode for solar water splitting, *Appl. Energy*, 2016, **164**, 924–933.

55 Y. Wang, B. Li, L. Zeng, D. Cui, X. Xiang and W. Li, Polyaniline/mesoporous tungsten trioxide composite as anode electrocatalyst for high-performance microbial fuel cells, *Biosens. Bioelectron.*, 2013, **41**, 582–588.